A99-16302

AIAA 99-0409
Hypersonic Boundary-Layer Receptivity to Freestream Disturbances Over an Elliptical Cross-Section Cone

Xiaolin Zhong and Haibo Dong
University of California, Los Angeles
Los Angeles, CA

37th Aerospace Sciences Meeting & Exhibit
January 11–14, 1999 / Reno, NV

HYPERSONIC BOUNDARY-LAYER RECEPTIVITY TO FREESTREAM DISTURBANCES OVER AN ELLIPTIC CROSS-SECTION CONE

Xiaolin Zhong *and Haibo Dong †
University of California, Los Angeles, California 90095

Abstract

Three-dimensional hypersonic boundary layers over non-axisymmetric cones involve cross flow instability and entropy layers between bow shocks and the bodies. In this paper, the receptivity of a 3-D hypersonic boundary layer to freestream acoustic disturbances is studied by numerical simulation of hypersonic flow over a 2:1 blunt elliptical cross-section cone. The receptivity studies are necessary for providing initial conditions for stability and transition studies of hypersonic boundary layers. Both steady and unsteady flow fields between the bow shock and the boundary layer are numerically simulated by using a 5th-order shock-fitting scheme to study the generation of instability waves in the boundary layer. The use of high-order shock fitting schemes makes it possible to study the physical interaction between the disturbance wave fields and the bow shock. The wave modes generated by the freestream disturbances are studied based on the simulation results. The paper also presents the results on validating the numerical method and computer code for simulations of 3-D hypersonic flow receptivity, stability, and transition with bow shock effects.

Introduction

The prediction of laminar-turbulent transition in hypersonic boundary layers is a critical part of the aerodynamic design and control of hypersonic vehicles [1]. In general, the transition is a result of nonlinear response of the laminar boundary layers to forcing disturbances [2]. In an environment with small initial disturbances, the path to transition consists of three stages: 1) receptivity, 2) linear eigenmode growth or transient growth, and 3) nonlinear breakdown to turbulence. The receptivity [3] of boundary layers to disturbances is the process of converting environmental disturbances into instability waves in the boundary layers. The receptivity mechanism provides important initial conditions in terms of amplitude, frequency, and phase for the instability waves in the boundary layers. The past theoretical, experimental, and numerical studies of boundary-layer receptivity were reviewed by Goldstein and Hultgren [4] and by Saric, Reed, and Kerschen [5]. Most theoretical results on incompressible boundary-layer receptivity have been obtained from the asymptotic analysis [6]. The asymptotic analysis explains how the long wavelength freestream acoustic disturbances enter a boundary layer and generate short-wavelength Tollmien-Schlichting (T-S) waves downstream of the leading edge. Recently, direct numerical simulation of the Navier-Stokes equations has become a powerful tool in the studies of stability and transition [7–9]. Examples of the DNS studies on the receptivity of low-speed boundary layers can be found in Refs. [10–16].

Despite several decades of research efforts, the stability and transition of hypersonic boundary layers is still currently not well understood [17,18]. Early works in hypersonic transition were mainly focused on the measurements of transition location in hypersonic boundary layers. Though they are valuable in deriving engineering correlations for transition locations, such measurements are not very useful in revealing the instability physics of hypersonic boundary layers. To overcome this drawback, hypersonic stability experiments were performed by many researchers. Examples of such experimental work on the stability characteristic of supersonic and hypersonic boundary layers are those by Laufer and Vrebalovich [19], Demetrides [20], Kendell [21], Stetson and Kimmel [22], Wilkinson and coworkers [23]. Recently, Poggie and Kimmel conducted experimental studies on the boundary layer transition at Mach 8 for an elliptic 2:1 cone [24].

We have been working on the the numerical simulation of hypersonic boundary-layer transition by developing high-order accurate numerical methods for direct numerical simulation [25,26], and we have developed and validated a set of fifth and seventh-order shock-fitting schemes for the DNS of practical hypersonic flows over blunt bodies. The use of the shock-fitting method makes it possible to accurately compute the physical bow-shock interactions, and the development of instability waves in the boundary layers. Subsequently, we [27] used the new schemes to conduct DNS studies of the receptivity of a hypersonic boundary layer to 2-D and axisymmetric freestream monochromatic planar acoustic disturbances for a Mach 15 flow over a parabolic leading edge. Local parallel linear stability analysis (LST) of the stability of the hypersonic bound-

*Associate Professor, Mechanical and Aerospace Engineering Department, e-mail: xiaolin@seas.ucla.edu, Member AIAA.
†Graduate Student, AIAA student member.

ary layer over the blunt wedge was also conducted [28] to compare with DNS results and to identify instability modes obtained by the DNS studies.

The objective of this paper is to study the receptivity of 3-D hypersonic boundary layers over 2:1 elliptical blunt bodies at Mach 15. The disturbances are freestream weak monochromatic planar acoustic waves. The receptivity studies are necessary for providing initial conditions for stability and transition studies of hypersonic boundary layers. Figure 1 shows a schematic of the wave field interactions near a hypersonic leading edge affected by freestream disturbances.

The receptivity for 3-D hypersonic flow over elliptical cones is a difficult problem affected by many interacting flow mechanisms. The uneven strength of the bow shock over the elliptical cone creates a circumferential pressure gradient. Such a pressure gradient generates inflectional cross flow velocity. It is expected inviscid inflectional instability will be an important effect on such flows. In addition, the receptivity of hypersonic boundary layers over blunt bodies is altered considerably by the presence of the bow shocks which are located very close to body surfaces at hypersonic Mach numbers. Stability and transition of hypersonic boundary layers are affected by nose bluntness and by the boundary-layer swallowing of entropy layers created by bow shocks [21,22,29]. For such complex unsteady flows, the direct numerical simulation is an ideal tool which is able to generate detailed flow field information useful to the understanding of the receptivity process. The numerical results on receptivity can provide initial conditions for hypersonic boundary stability and transition studies using the PSE approach.

In this paper, both steady and unsteady flow fields between the bow shock and the boundary layer are numerically simulated by using a 5th-order shock-fitting scheme to study the wave generation in the boundary layer. The wave modes generated by the freestream disturbances are studied based the simulation results. The paper also presents the results on validating the numerical method and computer code for simulations of 3-D hypersonic flow receptivity, stability, and transition with bow shock effects.

Equations and Numerical Methods

The governing equations and numerical methods are briefly summerized here. Details can be found in previous papers for 2-D flows [25,27]. The governing equations are the unsteady full three-dimensional Navier-Stokes equations written for the computation in the conservation-law form:

$$\frac{\partial U^*}{\partial t^*} + \frac{\partial F^*{}_j}{\partial x_j^*} + \frac{\partial F^*{}_{vj}}{\partial x_j^*} = 0 \qquad (1)$$

where superscript "$*$" represents dimensional variables, and

$$U^* = \{\rho^*,\ \rho^* u_1^*,\ \rho^* u_2^*,\ \rho^* u_3^*,\ e^*\} \qquad (2)$$

The gas is assumed to be thermally and calorically perfect. The viscosity and heat conductivity coefficients are calculated using Sutherland's law together with a constant Prandtl number, Pr. The equations are transformed into body-fitted curvilinear computational coordinates in a computational domain bounded by the bow shock and the body surface. The location and the movement of the bow shock is an unknown to be solved with the flow variables.

We nondimensionalize the velocities with respect to the freestream velocity U_∞^*, length scales with respect to a reference length d^* given by the body surface equation, density with respect to ρ_∞^*, pressure with respect to p_∞^*, temperature with respect to T_∞^*, time with respect to d^*/U_∞^*, vorticity with respect to U_∞^*/d^*, entropy with respect to C_p^*, wave number with respect to $1/d^*$, etc. The dimensionless flow variables are denoted by the same dimensional notation but without the superscript "$*$".

The numerical methods for spatial discretization of the 3-D full Navier-Stokes equations are a fifth-order shock-fitting scheme in streamwise and wall-normal directions, and a Fourier collocation method in the periodic spanwise flow direction for the case of a wedge geometry or in the azimuthal direction for the case of a cone geometry. The spatially discretized equations are advanced in time using a Low-Storage Runge-Kutta scheme of Williamson [30] of up to third order.

Receptivity Simulations

The numerical simulation for the receptivity of 3-D hypersonic flows over a blunt elliptical cone is carried out using our 3-D fifth-order shock fitting scheme where the outer grid line is the bow shock. The unsteady bow shock shape and shock oscillations are solved as part of the computational solution. Analytical formulas of the metric coefficients for coordinate transformation are used to ensure numerical accuracy for the unsteady coordinate transformation in the simulations. In the simulations, steady flow solutions are first obtained by advancing the unsteady flow computations to convergence using the fifth-order computer code. No disturbances are imposed in the freestream. The steady shock shape is obtained as a part of the numerical solution. Subsequently, unsteady viscous flows are computed by imposing a continuous planar acoustic single-frequency disturbance wave on the steady flow variables at the freestream side of the bow shock. The shock/disturbance interactions and generation of boundary waves are solved using the nonlinear Rankine-Hugoniot relations at the shock and the full Navier-Stokes equations in the flow fields. The unsteady calculations are carried out for about 15 to 30 periods in

time until the unsteady solutions reach a time periodic state. Finally, the unsteady computations are carried out for additional periods in time to perform FFT on the perturbation field to obtain the Fourier amplitudes and phase angles for the perturbations of the unsteady flow variables in the flow field.

The freestream disturbances are assumed to be weak monochromatic planar acoustic waves with wave front oblique to the center line of the body in the $x-z$ plane at an angle of ψ. The perturbations of flow variables in the freestream introduced by the freestream acoustic wave before reaching the bow shock can be written in the following form:

$$q'_\infty = |q'|_\infty \, e^{i(k\cos\psi\, x + k\sin\psi\, z - \omega t)} \qquad (3)$$

where $|q'|$ represents one of the flow variables, $|u'|$, $|v'|$, $|w'|$, $|p'|$, and $|\rho'|$. The freestream perturbation amplitudes satisfy the following relations:

$$|u'|_\infty = \epsilon\cos\psi\,, \qquad |v'|_\infty = 0\,,$$
$$|p'|_\infty = \gamma M_\infty \epsilon\,, \qquad |\rho'|_\infty = M_\infty \epsilon$$
$$|w'|_\infty = \epsilon\sin\psi$$

where ϵ represents the freestream wave magnitude. The angle ψ is the angle of freestream wave with respect to the x axis in the x-z plane, where $\psi = 0$ corresponds to 2-D planar waves. The parameter k is the dimensionless freestream wave number which is related to the dimensionless circular frequency ω by:

$$\omega = k\,(\cos\psi + M_\infty^{-1}) \qquad (4)$$

The dimensionless frequency F is defined as:

$$F = \frac{\omega^* \nu^*}{U_\infty^{*2}}\,. \qquad (5)$$

Code Validation

The 2-D and 3-D fifth-order shock fitting computer codes for the unsteady full Navier-Stokes equations have been extensively tested and validated for many steady and unsteady flow simulations. This paper presents the results of two test cases where numerical simulations are compared to published experimental bow shock shapes, surface presure, and heat transfer rates for axisymmetric and non-axisymmetric hypersonic flow over blunt cones. The numerical accuracy of the results are also evaluated by grid refinement studies.

Hypersonic Flow Over a Sphere

Axisymmetric laminar steady hypersonic flow over a sphere at zero angle of attack is computed using a three-dimensional grid. There are published experimental and numerical results for a sphere in supersonic flow [31,32] available for comparison. The flow conditions for the viscous flow computations are:

$M_\infty = 5.25$ and 7.4
$T^*_\infty = 192.989\,K$ $\qquad$ $p^*_\infty = 10.3\,Pa$
$T^*_w = 1000\,K$ $\qquad$ $\gamma = 1.4$
$Pr = 0.72$ $\qquad$ $d^* = 0.6\,m$
$Re_\infty = \rho^*_\infty U^*_\infty d^*/\mu^*_\infty = 36,159.3$

The body surface is assumed to be a non-slip wall with an isothermal wall temperature T^*_w. The viscosity is computed using the Sutherland's law for air. The results presented in this paper are obtained using 90 grid points in the streamwise direction and 60 points in the wall-normal direction. Since the flow is axisymmetric, only 4 Fourier collocation points are used in computing the azimuthal direction.

Figure 2 compares the computed and experimental [32] bow shock shapes for two test cases with freestream Mach numbers of 2 and 4. Our numerical results compare very well with the experimental results. Figure 3 shows the computed and experimental pressure coefficients for the case of freestream Mach number 7.4. The agreement is good. Grid refinement comparisons have also been done to verify that the grid is adequate for the viscous flow computations.

Heating Rates on a Blunt Elliptical Cone at Mach 10

We have also tested our 3-D Navier-Stokes code for 3-D non-axisymmetric flow over a blunt elliptical cone. The numerical results are compared with experimental results obtained by Hillsamer and Rhudy [33] and theoretical stagnation point heat-transfer results of Fay and Riddell [34]. Hillsamer and Rhudy [33] conducted heat-transfer and shadowgraph tests of several elliptical lifting bodies at Mach 10. Among their test models is configuration 30 shown in Fig. 4, considered in our numerical studies because it is similar to our elliptical cone configuration. Specifically, configuration 30 was a blunt elliptical cone with a major-to-minor axis ratio of 1.43:1. Basic dimensions for the model are shown in Fig. 5. In our simulation, the body shape is modeled by the following analytical formula:

$$(x-r)^2 + y^2 + z^2 = r^2 \qquad (6)$$

the section radius r is a function of (y,z), i.e.,

$$r^2 = \frac{y^2+z^2}{y^2/r_y^2 + z^2/r_z^2} \qquad (7)$$

where r_y and r_z are the nose radius of the major and minor axises respectively.

The laminar viscous flow over the same body is computed using the fifth-order shock-fitting scheme. The flow conditions for the viscous flow computations are:

$M_\infty = 10$ $\qquad$ $Re_\infty = 0.31 \times 10^6/\text{ft}$
$T_{0\infty} = 1061.11K$ $\qquad$ $T_w = 216.11\,K$
$\gamma = 1.4$ $\qquad$ $Pr = 0.72$
Nose Radius $r_y = 2.08in$ and $r_z = 2.97in$

The body surface is assumed to be a non-slip wall with an isothermal wall temperature. The viscosity is computed using the Sutherland's law for air. The results presented in this paper are obtained using a $92 \times 61 \times 32$ grid.

Fay and Riddell [34] did extensive stagnation line boundary layer calculations on stagnation heating rates. Fay and Riddell's result for the stagnation point heating coefficient h defined in the experimental studies are:

$$h = q_w/(T_e - T_w)$$
$$= 0.763\ Pr^{-0.6}\ c_p\ \sqrt{\rho_e \mu_e K}\ \left(\frac{\rho_w \mu_w}{\rho_e \mu_e}\right)^{0.1} \quad (8)$$

where K is the streamwise velocity gradient obtained approximately by the Newtonian theory for hypersonic flow at the stagnation point:

$$K = \frac{\partial u_e}{\partial x} = \frac{1}{R}\sqrt{\frac{2(p_e - p_\infty)}{\rho_e}} \quad (9)$$

For a non-axisymmetric elliptical cone, Reshotko [35] showed that the stagnation rates over an non-axisymmetric cold body can be evaluated by modifying the axisymmetric results based the major-to-minor axis ratio as

$$h = h_y \sqrt{(1 + \sqrt{\frac{r_y}{r_z}})/2} \quad (10)$$

where h_y is the axisymmetric heating rate obtained using the smaller radius r_y.

The Navier-Stokes solutions of stagnation heating rate is compared with experimental results and theoretical results. Hillsamer and Rhudy [33] did not use the modification of Reshotko [35]. They directly use the Fay and Riddle values with both the major and minor axises. The experimental result is expected to be bounded by the two sets of heating results. Figure 6 compares the computed, experimental, and theoretical results for configuration in Mach 10 flow and Reynolds number 0.31×10^6/ft. The numerical result agree very well with the experimental results. The experimental stagnation rates are slightly lower than the upper bound of the Fay and Riddell results, which agrees with the Reshotko modification formula.

Receptivity of Blunt Elliptical Cone at $M = 15$

As a first step in studying the receptivity of hypersonic boundary layers over elliptical cones, this paper considers a 2:1 blunt elliptical cone with a Mach 15 free stream. The specific test case is the receptivity to weak freestream acoustic disturbance waves by a Mach 15 hypersonic flow past an elliptical blunt cone at zero angle of attack. The body surface is specified by:

$$x^* = \frac{y^{*2}}{2r_y^*} + \frac{z^{*2}}{2r_z^*} - d^* \quad (11)$$

where r_y^* and r_z^* are the major and minor nose radius of curvatures. In the present simulations, the flow conditions are

$M_\infty = 15$ $\quad \epsilon = 1/3 \times 10^{-3}$
$T_{0\infty}^* = 5980\ K$ $\quad T_w^* = 1000\ K$
$\gamma = 1.4$ $\quad Pr = 0.72$
Nose Radius $r_y^* = .0125m$ and $r_y^* : r_z^* = 2:1$
Reference length $d^* = 0.01m$
$Re_\infty = 0.60266 \times 10^5$/m

The body surface is assumed to be a non-slip wall with an isothermal wall temperature T_w^*.

The numerical simulations are carried out in an IBM SP-2 parallel computer. So far, only one test case for flow near the nose region and one unsteady case with freestream dimensionless frequency of the disturbance wave $F \times 10^6 = 4274$ has been computed and presented in this paper. The results presented in this paper are obtained using two sets of grids: $92 \times 31 \times 64$ and $92 \times 61 \times 64$ grids. There are no experimental results available for comparison for the numerical solutions of the present test cases. There are theoretical results on the stagnation point heating rates and the theoretical inviscid results on vorticity jump across curved bow shock. These results will be used to compare with numerical solutions.

Steady Flow Solutions

Figure 7 shows the steady solution for a set of $92 \times 31 \times 64$ computational grid obtained by the simulation. The steady bow shock shape is the outer computational boundary. The 3-D steady solutions for Mach number contours are shown in Fig. 8. The uneven strength of the bow shock in the major and minor axises create the circumferential pressure gradient and cross flow velocity. The cross mass flow thickens the boundary in the minor z axis and enlarge the standoff distance there. The bow shock and development of boundary layers along the body surface are shown in Fig. 9 for the velocity vectors in two cross sections along the major and minor axis. The figure also shows that the boundary layer along the minor (z) axis is thicker than that along the major (y) axis due to the cross flow effect.

Similar to the validation case, the stagnation point heating rate is compared with theoretical results of Fay and Riddell. The computational and theoretical results are summarized in Table 1. The agreement between the two sets of results is very good.

Table 1. Computed and theoretical stagnation-point heating coefficient

Grid	N-S Calculations	Fay & Riddell
92×31×32	.016804	.016324
92×61×64	.016802	.016324

The effect of cross flow is examined in more details by study the vorticity, velocity, and pressure distribution in the circumferential direction. Figure 10 shows the computational grid in a $x = constant$ cross section. The circumferential grid index k is marked in the figure. A local body fitted coordinates (s, n, ϕ) with unit vectors $(\mathbf{e}_1, \mathbf{e}_2, \mathbf{e}_3)$ are defined to compute velocity and vorticity components, where $\mathbf{e}_2$ is the wall normal direction, $\mathbf{e}_3$ is the circumferential direction which is normal to a $k = constant$ grid surface, and $\mathbf{e}_1 = \mathbf{e}_2 \times \mathbf{e}_3$ defines the streamwise direction. The cross flow generates streamwise vorticity component in the shock layer. Fig. 11 shows the contours of streamwise vorticity components in a x =constant grid station. The figure shows that the vorticity is generated by cross flow velocity on the wall. In addition, according the Crocco's theorem, the curved bow shock also generates an entropy gradient and inviscid vorticity behind the shock. The inviscid vorticity jump across the bow shock was derived by Truesdell [36], Lighthill [37], and by Hayes [38] using the Rankine-Hugoniot relation and Crocco's theorem or momentum equation in the direction normal to the shock. For a bow shock in a uniform freestream flow, the vorticity vector behind the shock depends only on the density ratio across the shock and the shock curvature tensor, i.e.,

$$\vec{\omega}_{\text{shk}} = \frac{(1 - \rho_\infty/\rho_s)^2}{\rho_\infty/\rho_s} (\vec{n} \times \vec{u_s} \cdot \mathbf{K}) \qquad (12)$$

where $\mathbf{K} = \nabla \vec{n}$, $\vec{u_s}$ is tangential velocity at the shock, and $\vec{n}$ is the shock unit normal vector. The equation above can be used to compare the vorticity vector behind the shock using numerically obtained shock curvature. Fig. 12 shows the vorticity components immediately behind the bow shock at the $x = -0.55$ grid station. The inviscid theoretical results computed by Eq. (12) agree reasonably well with viscous numerical solutions. The differences are due to viscous effects are not accounted for in Eq. (12). It is expected the two results will agree better when the shock layer is separated with the boundary layer as the shock is moving away from the boundary layer farther downstream. This can be shown in Fig. 13. The two sets of solutions approach each other as the location moves downstream (increasing x).

The cross-flow, wall-normal, and streamwise velocity distributions along wall normal directions for several k grid lines located at the $x = -0.55$ grid station are shown in Figs. 14 to 16. The η coordinate is the wall-normal distance normalized by local shock standoff distance. Figure 14 shows that there are cross flow inflection points near the shoulder of the major y axis. As the k increases, the inflection point moves away from the wall. The maximum cross flow velocity appears also near the shoulder of the major y axis as shown in Fig. 17. Figure 14 shows the cross flow creates negative displacement velocity in the major axis and positive displacement in the minor axis. The boundary layer in the minor axis is much thinner than that in the major axis. Figure 14 shows the stream velocity components do not vary very much in the circumferential direction, but the Mach number changes more dramatically in the circumferential direction due to the temperature changes.

For compressible boundary layers over flat plates, Lin and Lees [39] showed that a generalized inflection point for inviscid instability corresponds to the zeros of $d(\rho du_\phi/dn)/dy$. Figures 18 and 19 show the variation of $\rho(du_\phi/dn)$ at the $x = -0.55$ grid station. Their generalized inflection points are in the middle of the shock layers which is outside of the boundary. It is expected there is inviscid inflectional instability in the inviscid shock layer due to cross flow effects.

Finally, Fig. 20 shows the steady flow streamlines in a $j = 5$ grid surface near the body surface. The cross flow can be seen in the figure.

Unsteady Flow Solutions

Having obtained the steady flow solutions, the generation of boundary-layer waves by freestream acoustic disturbances is simulated for 3-D hypersonic flow over a blunt elliptical cone with a freestream disturbance wave of dimensionless frequency $F \times 10^6 = 4247.9$.

Figure 21 shows the 3-D contours for the instantaneous entropy perturbation s' after the unsteady computations are carried out for enough periods in time that periodic solutions have been reached in the entire flow field. Figures 22 and 23 show instantaneous entropy and pressure perturbations in the major and minor axises. The instantaneous contours show the development of a single wave mode in the boundary layer along the surface. Due to the limit in the length of the computational domain of the present case, only a single mode is developed in the flow field. Work is underway to carry out the receptivity process further downstream by using successive overlapped zones. Such an approach is possible because the waves are convective waves propagating downstream. The figures also show that the entropy wave structure is more complex than that for the pressure perturbations. The possible reason is due to the effects of the entropy layer and its interaction with the boundary layer.

Figures 24 and 25 show instantaneous streamwise velocity perturbations immediately behind the bow shock and on the body surface along the major ($k = 1$) and minor ($k = 17$) axises. While the wave propagates with almost the same speed behind the shock, the wave propagate faster along the major axis ($k = 1$) than along the minor axis ($k = 17$) On the other hand, the wave strength is stronger near the minor axis. Such uneven wave speed and wave amplitudes can also be shown in Fig. 26.

The phase angles obtained by performing temporal FFT on perturbation variables are useful in understand-

ing the process of wave propagation in the flow field. If the disturbance is dominated by a single harmonic wave, the wave number and speed can be obtained from the phase angle by

$$\alpha_r = |\frac{d\phi}{dx}| \tag{13}$$

where α_r is dimensionless wave number, the dimensionless wave speed can be calculated by $c = \frac{\omega}{\alpha_r}$. Therefore, the slope in the phase determined the wave speeds and wave numbers of the waves. Figures 27 and 28 show the contours of entropy perturbations phase angles and amplitudes along the body surface.

Figures 29 and 30 show the contours of the Fourer phase angles for pressure and entropy in a cross section along the minor ($y = 0$) axis. The smooth increase of pressure phase angles behind the shock shows that the disturbance waves in the region immediately behind the shock are dominated by the forced interaction of the waves with the bow shock. On the other hand, the contours of the pressure phase angles show that in the leading edge region, there is very little pressure phase distortion in the wall-normal direction caused by the effect of the viscous boundary layers. The contours of the entropy phase angles show much more complex patterns. The figure shows that there is a viscous layer developing in the boundary layer. Figure 31 shows the distribution of entropy perturbation phase angles along the minor axises. The slopes of the phase angle on the body surface and behind the shock show that the wave speed is smaller on the body surface.

Figures 32 to 34 show the profiles of $|s'|$ amplitudes along the streamwise and circumferential directions. The results show that there is a strong development of disturbances near the body surface in terms of disturbance amplitudes. The distribution of pressure and temperature perturbation amplitudes along wall normal directions for several k grid lines located at the $x = -0.55$ grid station are shown in Figs. 35 and 36. The shapes of the amplitude profiles do not change very much in the circumferential direction.

Conclusions

The receptivity of 3-D hypersonic boundary layers to freestream acoustic disturbances has been studied by the numerical simulation of Mach 15 mean flows over a blunt 2:1 elliptical cone. The main conclusions are:

1. We have developed and validated our numerical method and computer code for simulations of 3-D hypersonic flow receptivity with bow shock effects. The numerical results compared very well with experimental ones of bow shock shapes, surface pressure, and stagnation heating rates for hypersonic flow over symmetric and non-symmetric blunt cones.

2. Steady flow solution for Mach 15 flow over the 2:1 elliptical cone shows the secondary flow with inflection points created by the uneven strength of the bow shock.

3. Unsteady receptivity solutions are generated and analyzed for one test case. The receptivity simulation results show that new schemes can resolve 3-D transient hypersonic flow with physical bow-shock oscillations accurately.

4. Future work include: parametric studies on the effects of Mach numbers, Reynolds numbers, wall cooling, nose bluntness, surface curvature, and the entropy layers on the receptivity; comparison with local linear theory and couple receptivity results with 3-D PSE calculations.

Acknowledgments

This research was supported by the Air Force Office of Scientific Research under grant numbers F49620-95-1-0405 and F49620-97-1-0030 monitored by Dr. Len Sakell.

References

[1] Defense Science Board, "Final Report of the Second Defense Science Board Task Force on the National Aero-Space Plane (NASP)," *AD-A274530, 94-00052, November*, 1992.

[2] Reshotko, E., "Boundary Layer Instability, Transition and Control," *AIAA paper 94-0001*, 1996.

[3] Morkovin, M., "On the Many Faces of Transition," *Viscous Drag Reduction*, edited by C. Wells, Plenum, 1969, pp. 1–31.

[4] Goldstein, M. E. and Hultgren, L. S., "Boundary-Layer Receptivity to Long-Wave Free-Stream Disturbances," *Annual Review of Fluid Mechanics*, Vol. 21, pp. 137-166 1989.

[5] Saric, W. S., Reed, H. L., and Kerschen, E. J., "Leading Edge Receptivity to Sound: Experiments, DNS, and Theory," *AIAA Paper 94-2222*, 1994.

[6] Goldstein, M. E., "The evolution of Tollmien-Schlichting Waves near a Leading Edge," *Journal of Fluid Mechanics*, Vol. 127, pp. 59-81 1983.

[7] Kleiser, L. and Zang, T. A., "Numerical Simulation of Transition in Wall-Bounded Shear Flows," *Ann. Rev. Fluid Mech.*, Vol. 23, 1991, pp. 495–535.

[8] Reed, H. L., "Direct Numerical Simulation of Transition: the Spatial Approach," *Progress in Transition Modeling*, AGARD-Report-793 1994.

[9] Pruett, C. D., Zang, T. A., Chang, C.-L., and Carpenter, M. H., "Spatial Direct Numerical Simulation of High-Speed Boundary-Layer Flows, Part I: Algorithmic Considerations and Validation," *Theoretical and Computational Fluid Dynamics*, Vol. 7, 1995, pp. 49–76.

[10] Murdock, J. W., "Tollmien-Schlichting Waves Generated by Unsteady Flow over Parabolic Cylinders," *AIAA paper 81-0199*, 1981.

[11] Lin, N., Reed, H. L., and Saric, W. S., "Effect of Leading-Edge Geometry on Boundary-Layer Receptivity to Freestream Sound," *Instability, Transition, and Turbulence*, Vol. M. Y. Hussaini et al., editors, pp. 421-440, Springer-Verlag, 1992.

[12] Buter, T. A. and Reed, H. L., "Boundary Layer Receptivity to Free-Stream Vorticity," *Physics of Fluids*, Vol. 6, No. 10, 1994, pp. 3368–3379.

[13] Casalis, G. and Cantaloube, B., "Receptivity by Direct Numerical Simulation," *Direct and Large-Eddy Simulation I*, Vol. P. R. Voke et al., editors, pp. 237-248, Kluwer Academic Publishers, 1994.

[14] Collis, S. S. and Lele, S. K., "A Computational Approach to Swept Leading-Edge Receptivity," *AIAA paper 96-0180*, 1996.

[15] Corke, T. C. and Haddad, O., "Receptivity to sound on a parabolic leading edge," *In Transitional Boundary Layers in Aeronautics*, Vol. Edited by R.A.W.M. Henkes and J. L. van Ingen, pp. 403-412, North-Holland, Amsterdam, 1996.

[16] Liu, Z., Xiong, G., and Liu, C., "Receptivity to Freestream Vortical Disturbance of 2D and 3D Airfoils," *AIAA paper 96-2084*, January 1996.

[17] Reshotko, E., "Hypersonic Stability and Transition," *in Hypersonic Flows for Reentry Problems, Eds. J.-A. Desideri, R. Glowinski, and J. Periaux, Springer-Verlag*, Vol. 1, 1991, pp. 18–34.

[18] Morkovin, M. V., "Transition at Hypersonic Speeds," *ICASE Interim Report 1*, Vol. NASA CR 178315, May, 1987.

[19] Laufer, J. and Vrebalovich, T., "Stability and Transition of a Supersonic Laminar Boundary Layer on a Insulated Flat Plate," *Journal of Fluid Mechanics*, Vol. Vol. 9, part 2, pp. 257–294, 1960.

[20] Demetriades, A., "Laminar Boundary Layer Stability Measurements at Mach 7 Including Wall Temperature Effects," *AFOSR-TR-77-1311*, Vol. November, 1977.

[21] Kendall, J. M., "Wind Tunnel Experiments Relating to Supersonic and Hypersonic Boundary-Layer Transition," *AIAA Journal*, Vol. Vol. 13, No. 3, pp. 290–299, 1975.

[22] Stetson, K. F. and Kimmel, R. L., "On Hypersonic Boundary Layer Stability," *AIAA paper 92-0737*, 1992.

[23] Wilkinson, S., "A Review of Hypersonic Boundary Layer Stability Experiments in a Quite Mach 6 Wind Tunnel," *AIAA Paper 97-1819*, 1997.

[24] Poggie, J. and Kimmel, R. L., "Traveling Instabilities in Elliptic Cone Boundary Layer Transition at Mach 8," *AIAA paper 98-0435*, January 1998.

[25] Zhong, X., "Direct Numerical Simulation of Hypersonic Boundary-Layer Transition Over Blunt Leading Edges, Part I: New Numerical Methods and Validation (Invited)," *AIAA paper 97-0755, 35th AIAA Aerospace Sciences Meeting and Exhibit, January 6-9, Reno, Nevada*, 1997.

[26] Zhong, X., "High-Order Finite-Difference Schemes for Numerical Simulation of Hypersonic Boundary-Layer Transition," *Journal of Computational Physics*, Vol. 144, August 1998, pp. 662–709.

[27] Zhong, X., "Direct Numerical Simulation of Hypersonic Boundary-Layer Transition Over Blunt Leading Edges, Part II: Receptivity to Sound (Invited)," *AIAA paper 97-0756*, January 1997.

[28] Hu, S. H. and Zhong, X., "Linear Stability of Compressible Couette Flow," *AIAA paper 97-0432*, January 1997.

[29] Reshotko, E. and Khan, N. M. S., "Stability of the Laminar Boundary Layer on a Blunt Plate in Supersonic Flow," *IUTAM Symposium on Laminar-Turbulent Transition*, edited by R. Eppler and H. Fasel, Springer-Verlag, Berlin, 1980, pp. 186–190.

[30] Williamson, J. H., "Low-Storage Runge-Kutta Schemes," *Journal of Computational Physics*, Vol. 35, 1980, pp. 48–56.

[31] Kopriva, D. A., "Multidomain Spectral Solutions of High-Speed Flows over Blunt Cones," *AIAA Journal*, Vol. 31, No. 12, 1993.

[32] Cleary, J. W., "An Experimental and Theoretical Investigation of the Pressure Distribution and Flowfields of Blunted Cones at Hypersonic Mach Numbers," NASA TN D-2969 1965.

[33] Hillsamer, M. E. and Rhudy, J. P., "Heat-Transfer and Shadowgraph Tests of Several Elliptical Lifting Bodies at Mach 10," *AEDC Report*, Vol. AEDC-TDR-64-19, 1964.

[34] Fay, J. A. and Riddell, F. R., "Theory of Stagnation Point Heat Transfer in Dissociated Air," *Journal of the Aeronautical Sciences*, Vol. 25, 1958, pp. 73–85.

[35] Reshotko, E., "Heat Transfer to a General Three-Dimensional Stagnation Point," *Journal of American Rocket Society*, January.

[36] Truesdell, C., "On the curved shocks in steady plane flow of an ideal fluid," *Journal of Aero. Sciences*, Vol. 19, 1952, pp. 826–828.

[37] Lighthill, M. J., "Dynamics of a Dissociating Gas. Part I. Equilibrium Flow," *Journal of Fluid Mechanics*, Vol. 2, No. 1, 1957, pp. 1.

[38] Hayes, W. D., "The vorticity jump across a gasdynamic discontinuity," *Journal of Fluid Mechanics*, Vol. 26, 1957, pp. 433–436.

[39] Lees, L. and Lin, C. C., "Investigation of the Stability of the Laminar Boundary Layer in Compressible Fluid," *NACA TN No. 1115*, 1946.

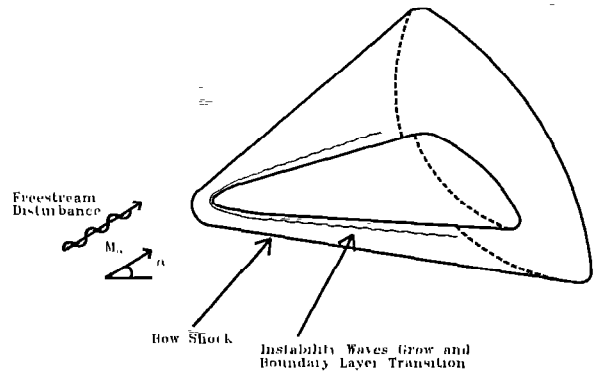

Figure 1: Hypersonic flow field in the direct numerical simulation of 3-D reacting hypersonic boundary-layer transition and receptivity to free-stream disturbances over a blunt elliptic cross-section cone.

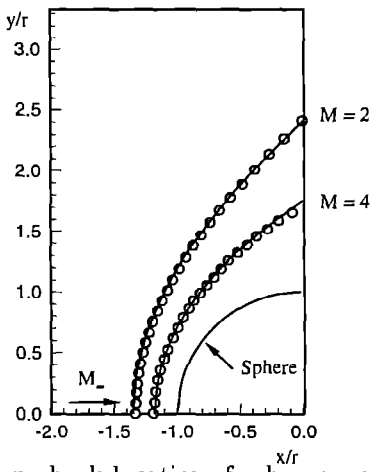

Figure 2: Bow shock locations for hypersonic flow over a sphere (lines: Navier-Stokes solutions, circles: experiments [Cleary 1965]).

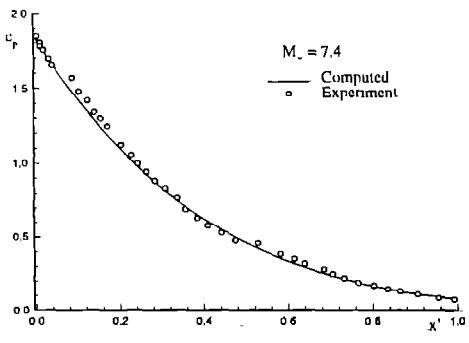

Figure 3: Pressure coefficients on the sphere surface (lines: Navier-Stokes solutions, circles: experiments [Cleary 1965]).

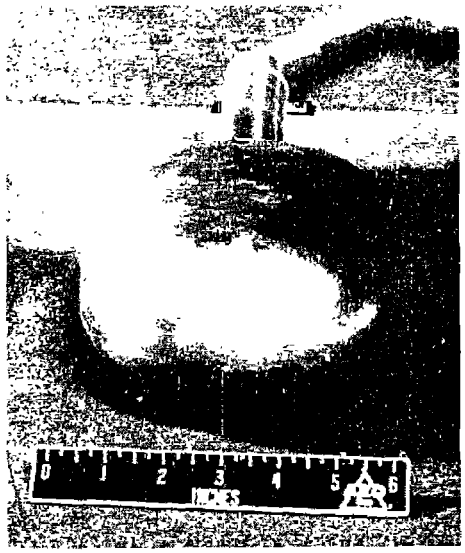

Figure 4: Photograph of model configuration 30 used in experimental studies of Hillsamer and Rhudy (taken from [Hillsamer and Rhudy 1964]).

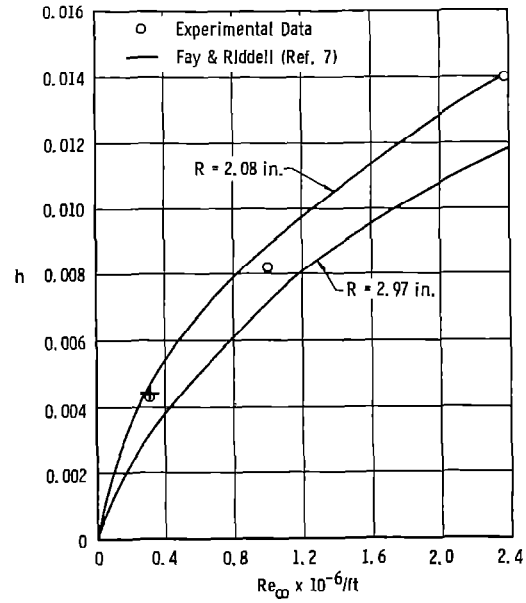

Figure 6: Comparison of numerical (shown by a + symbol) with experimental and theoretical stagnation point heat-transfer coefficient (in Btu/ft^{2}sec$^\circ R$) for the 1.43:1 blunt elliptical cone at Mach 10.

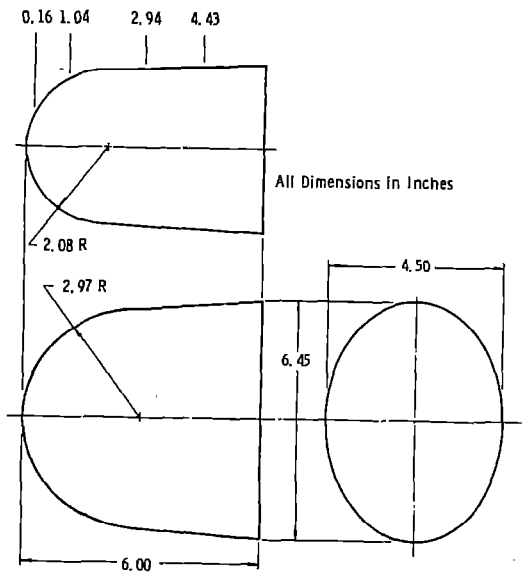

Figure 5: Basic dimensions for configuration 30 used in experimental studies of Hillsamer and Rhudy (taken from [Hillsamer and Rhudy 1964]).

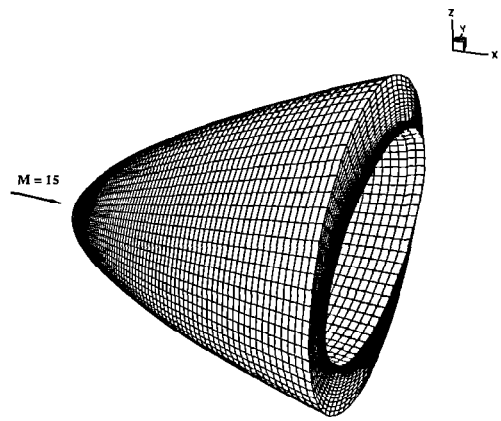

Figure 7: Computational grid for the numerical simulation of the receptivity of a 3-D Mach 15 flow over a blunt elliptical cone.

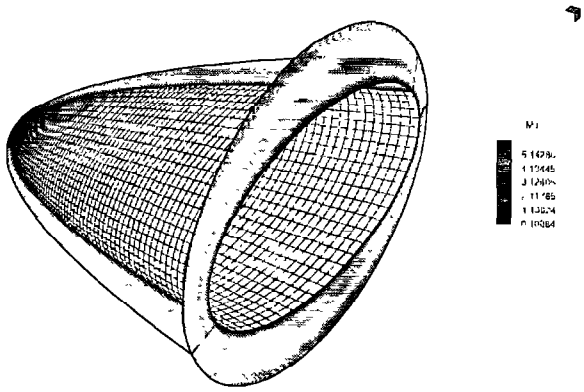

Figure 8: 3-D Mach number contours for Mach 15 flow over the elliptical blunt cone.

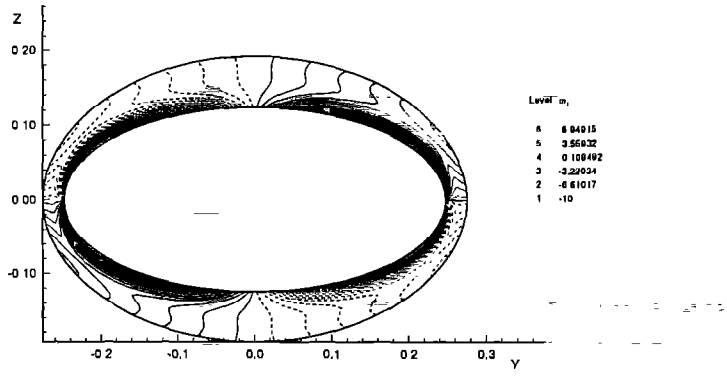

Figure 11: Contours of streamwise vorticity components at the $x = -0.55$ grid station.

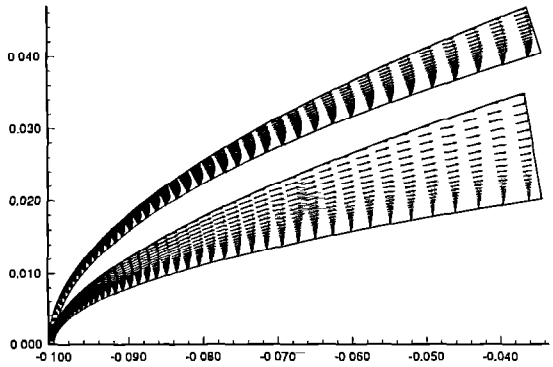

Figure 9: Velocity vectors of steady solutions for Mach 15 flow over the elliptical blunt cone in the major and minor axises.

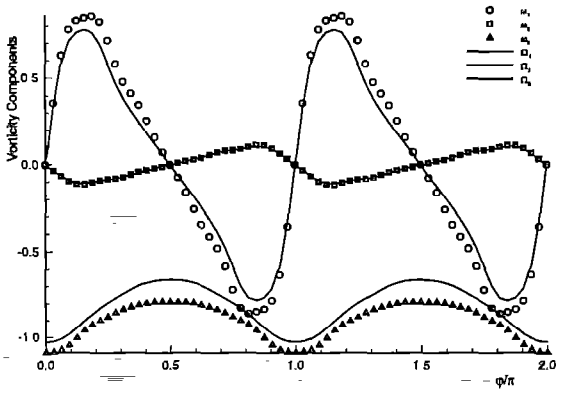

Figure 12: Vorticity components immediately behind the bow shock at the $x = -0.55$ grid station (inviscid theoretical results: ω_i; viscous numerical solutions: Ω_i).

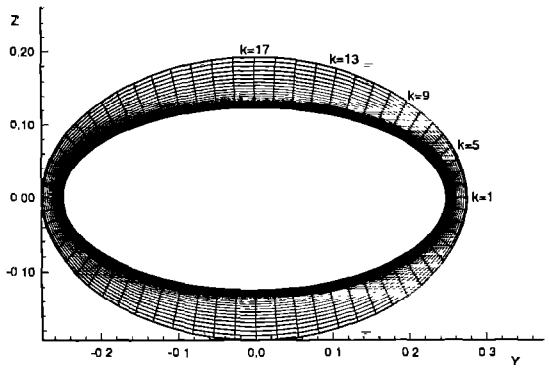

Figure 10: Computational grids at a x =constant grid stations, where the bow shock shape is the outer boundary.

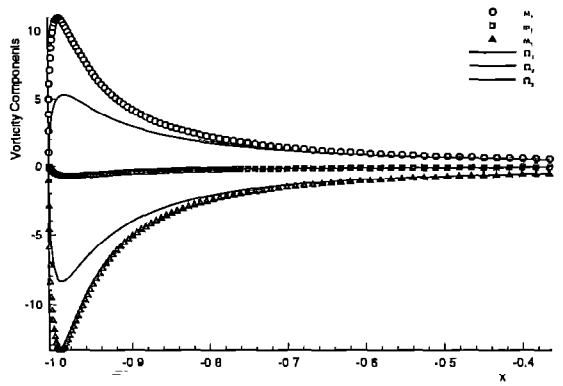

Figure 13: Comparison of theoretical and numerical vorticity components immediately behind the bow shock at a $k = 7$ grid station.

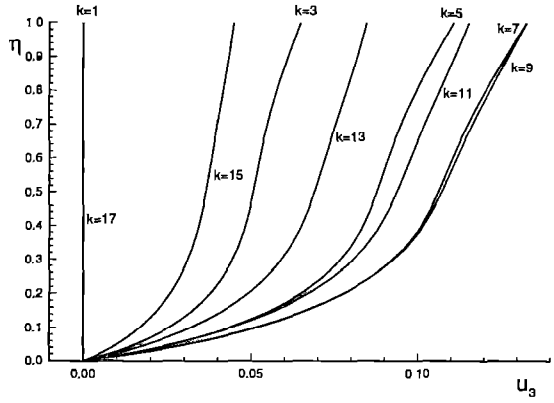

Figure 14: Cross-flow (circumferential) velocity distribution along wall normal direction for several k grid lines located at the $x = -0.55$ grid station.

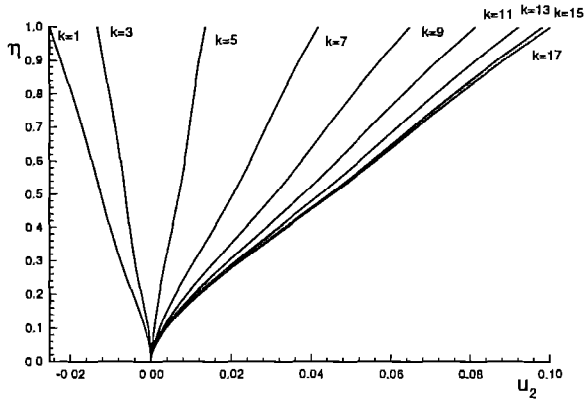

Figure 15: Wall-normal velocity distribution along wall normal direction for several k grid lines located at the $x = -0.55$ grid station.

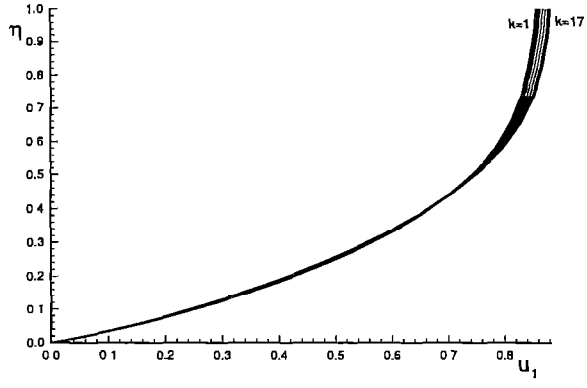

Figure 16: Streamwise velocity distribution along wall normal direction for several k grid lines located at the $x = -0.55$ grid station.

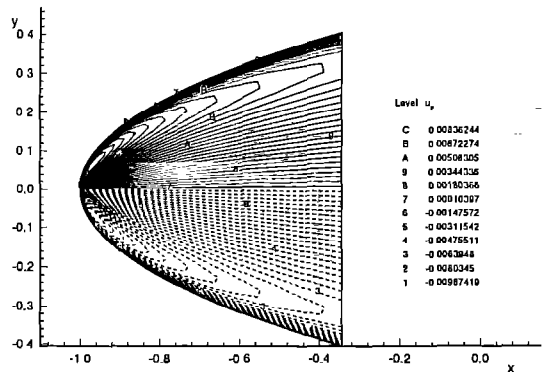

Figure 17: Contours of cross-flow (circumferential) velocity components in a j constant grid surface near the body surface.

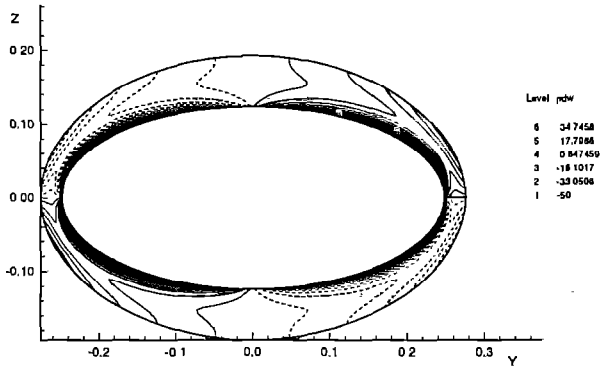

Figure 18: Contours of $\rho du_\phi/dn$ at the $x = -0.55$ grid station.

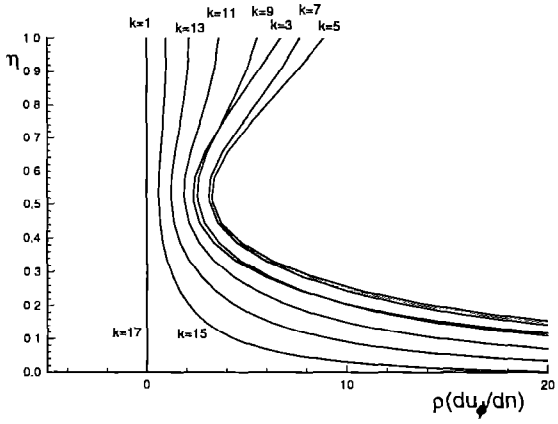

Figure 19: Distribution of $\rho du_\phi/dn$ along wall normal directions for several k grid lines located at the $x = -0.55$ grid station.

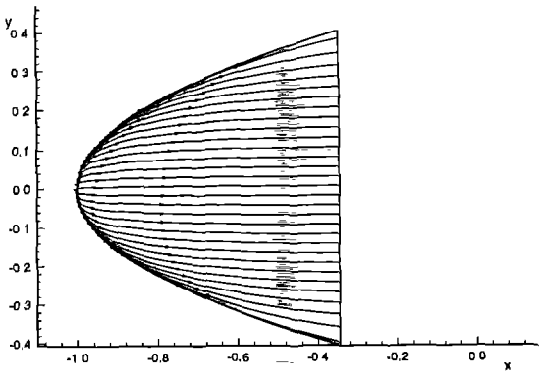

Figure 20: Streamlines in a $j = 5$ grid surface near the body surface.

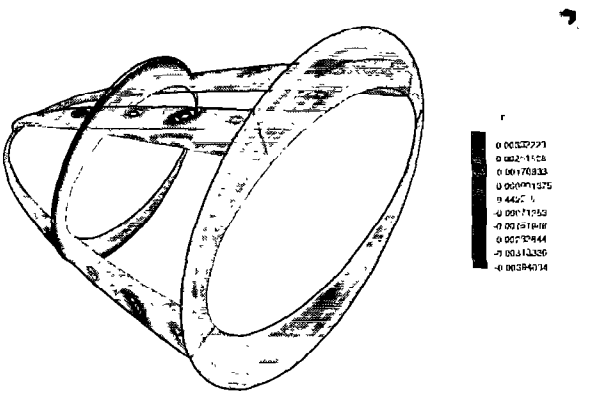

Figure 21: Instantaneous 3-D entropy perturbations induced by freestream planar acoustic disturbances.

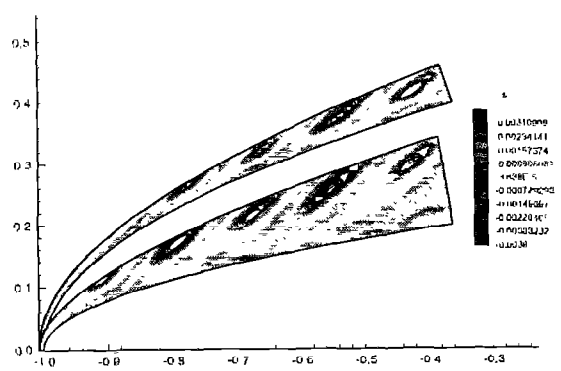

Figure 22: Instantaneous entropy perturbations induced by freestream planar acoustic disturbances in the major and minor axises.

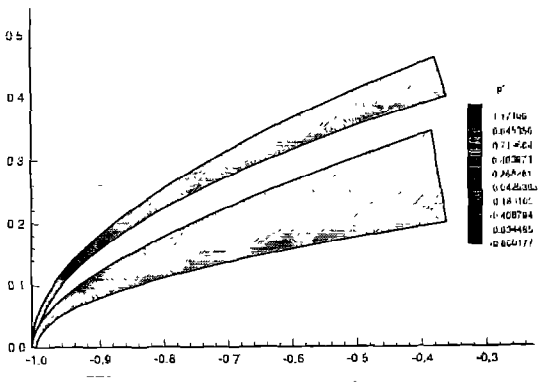

Figure 23: Instantaneous pressure perturbations induced by freestream planar acoustic disturbances in the major and minor axises.

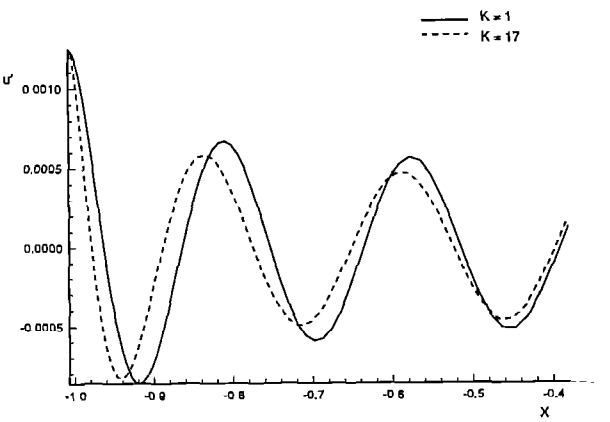

Figure 24: Instantaneous streamwise velocity perturbations immediately behind the bow shock along the major ($k = 1$) and minor ($k = 17$) axises.

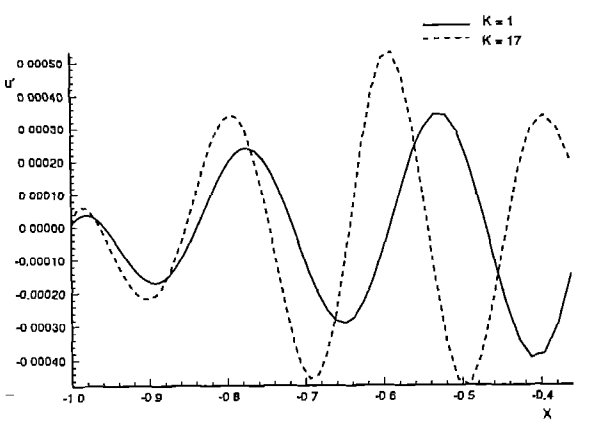

Figure 25: Instantaneous streamwise velocity perturbations on $j = 5$ grid line near body surface along the major ($k = 1$) and minor ($k = 17$) axises.

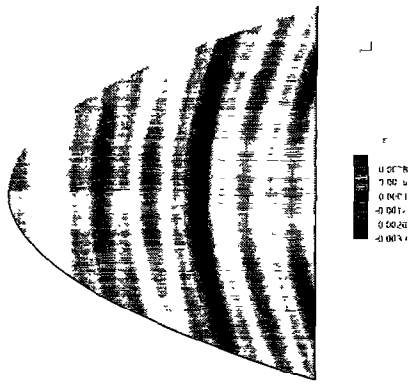

Figure 26: Contours of instantaneous entropy perturbations on body surface in the $x - y$ plane.

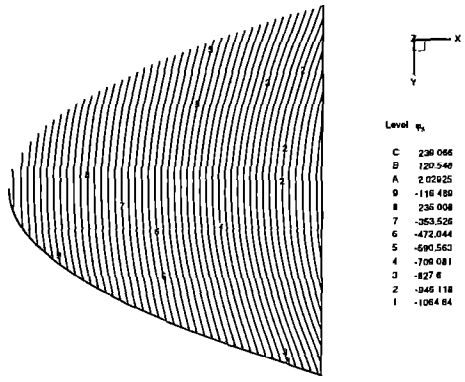

Figure 27: Contours of entropy perturbation phase angles on body surface in the $x - y$ plane.

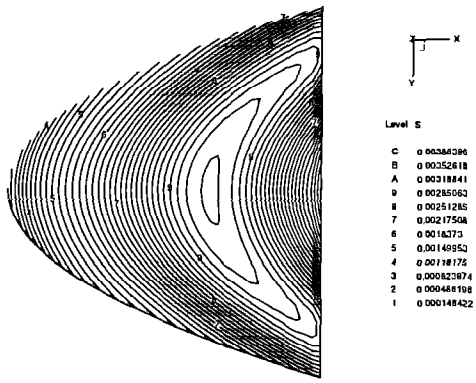

Figure 28: Contours of entropy perturbation amplitudes on body surface in the $x - y$ plane.

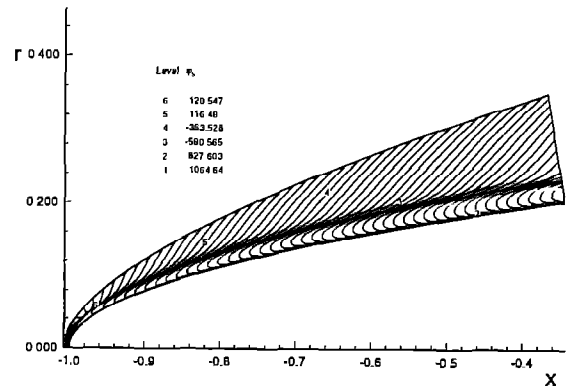

Figure 29: Contours of entropy perturbation phase angles induced by freestream planar acoustic disturbances in a cross section along the minor ($y = 0$) axis.

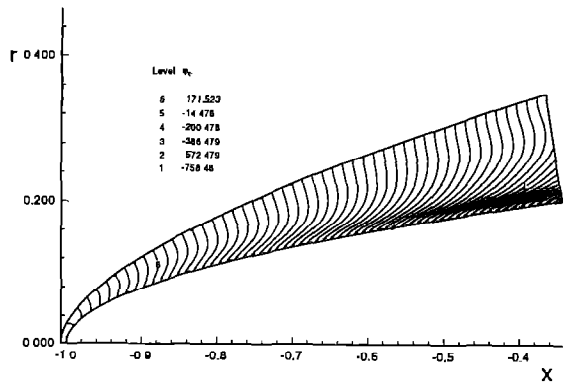

Figure 30: Contours of pressure perturbation phase angles induced by freestream planar acoustic disturbances in a cross section along the minor ($y = 0$) axis.

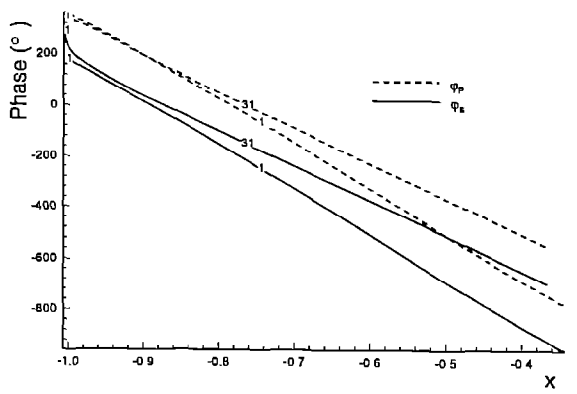

Figure 31: The distribution of pressure and entropy perturbation phase angles along the minor axises (label 1: on body surface, 31: immediately behind shock).

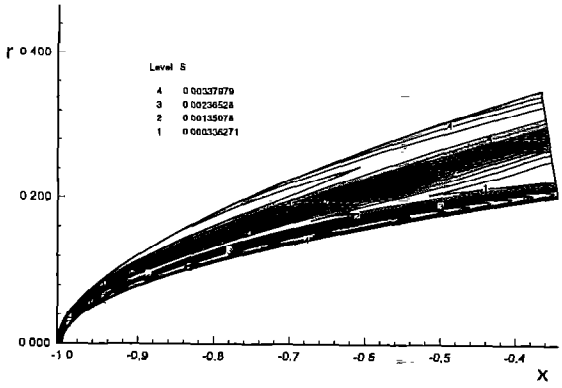

Figure 32: Contours of entropy perturbation amplitudes induced by freestream planar acoustic disturbances in a cross section along the minor ($y = 0$) axis.

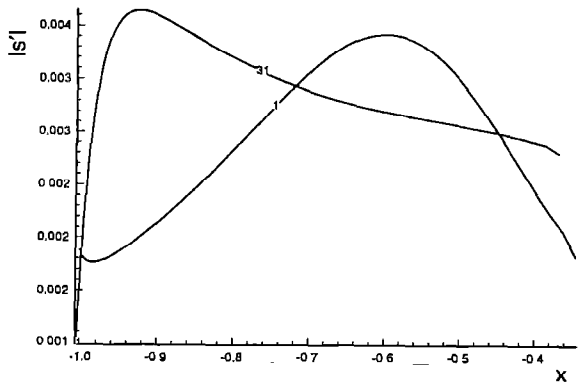

Figure 33: The distribution of entropy perturbation amplitudes along the minor axises (label 1: on body surface, 31: immediately behind shock).

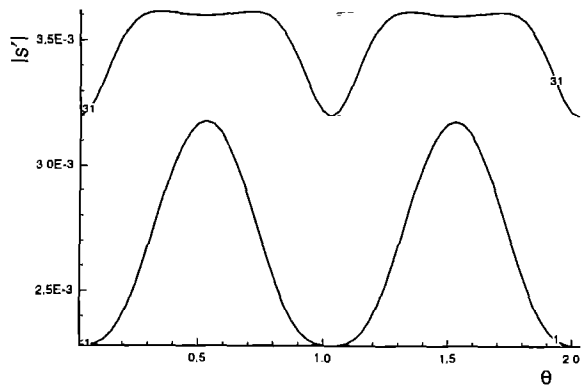

Figure 34: Distribution of entropy perturbation amplitudes in the circumferential direction at the $x = -0.55$ grid station (label 1: on body surface, 31: immediately behind shock).

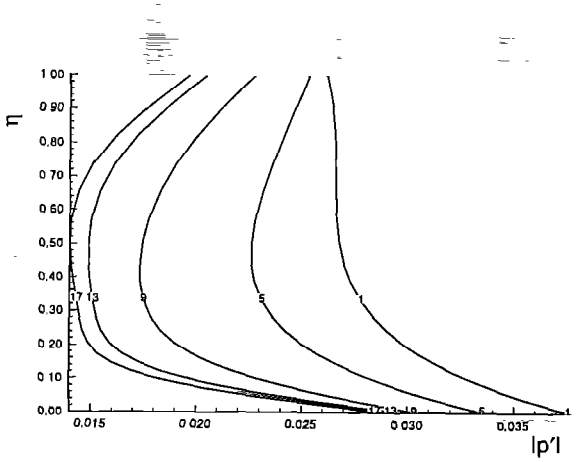

Figure 35: Distribution of pressure perturbation amplitudes along wall normal direction for several k grid lines located at the $x = -0.55$ grid station.

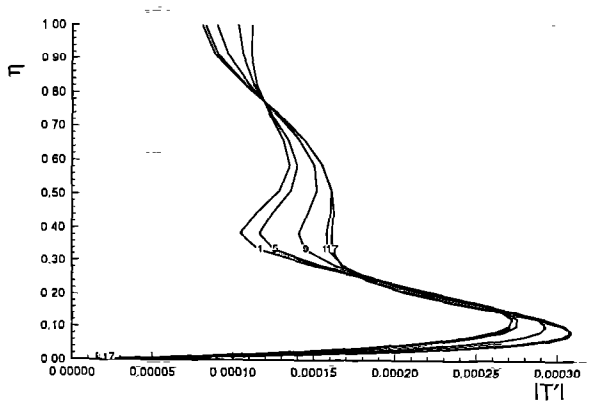

Figure 36: Distribution of temperature perturbation amplitudes along wall normal direction for several k grid lines located at the $x = -0.55$ grid station.